Available online at www.sciencedirect.com
SCIENCE DIRECT®
Aerosol Science 37 (2006) 677–695
Journal of Aerosol Science
www.elsevier.com/locate/jaerosci

# Quantitative laser-induced breakdown spectroscopy for aerosols via internal calibration: Application to the oxidative coating of aluminum nanoparticles

D. Mukherjee, A. Rai, M.R. Zachariah*

*Department of Mechanical Engineering, and Department of Chemistry and Biochemistry, University of Maryland, College Park, MD 20852, USA*

Received 21 December 2004; received in revised form 4 May 2005; accepted 4 May 2005

**Abstract**

We present a methodology for the quantitative use of laser-induced breakdown spectroscopy (LIBS) for the compositional characterization of nanoaerosols, using an internal standard. The approach involves finding the optimal laser delay time to collect spectra for each of the elemental species of interest, and measuring the plasma temperature, and background gas density under the same conditions. This enabled us to eliminate effects due to different experimental conditions, species excitation from different energy states, temporal evolution of the plasma volume itself and instrumental collection efficiencies and biases.

We apply the method to the problem of determining the extent of oxidation or coating thickness of aluminum nanoparticles. The specific choice of system is based on a need to understand the nature of energetic properties of nano-materials and in particular the reactivity and stability of passivation coatings, such as metal oxides.

The present work establishes LIBS as an effective analytical tool for quantitative estimation of the extent of oxidation in Al nanoparticles from time-resolved atomic emission spectra. More generically this approach of using the background gas as the internal standard mitigates the need for the use of materials standards and should be extendable to the characterization of other multi-component aerosol systems.


*Keywords:* LIBS; Quantitative analysis; Oxidation; Al nanoparticles

* Corresponding author. Tel.: +1 301 405 4311; fax: +1 301 314 9477.
*E-mail address:* mrz@umd.edu (M.R. Zachariah).

0021-8502/$ - see front matter © 2005 Elsevier Ltd. All rights reserved.
doi:10.1016/j.jaerosci.2005.05.005

## 1. Introduction

Laser-induced breakdown spectroscopy (LIBS) involves the collection and processing of the spectral signature resulting from a high-irradiance pulsed laser generated plasma containing an analyte (Radziemski & Cremers, 1989). The generic nature of the breakdown has been actively pursued as a robust and conceptually simple method for the elemental characterization of gases, solids, liquids and aerosols. A large volume of literature is available on the various applications of LIBS beginning with the breakdown of air (Damon & Thomlinson, 1963; Meyerand & Haught, 1963; Minck, 1964), to the physics of LIBS for characterizing the nature of the breakdown process itself (Weyl, 1989). The advent of advanced and more reliable lasers, spectrometers and high-sensitivity cameras has enabled the wide application of LIBS in carrying out elemental and spectral analysis of gases (Yalcin, Crosley, Smith, & Faris, 1999; Radziemski, Loree, Cremers, & Hoffman, 1983; Hanafi, Omar, & Gamal, 2000), solids (Lee, Thiem, Kim, Teng, & Sneddon, 1992; Kim, Yoo, Park, Oh, & Kim, 1997) and aerosols (Martin & Cheng, 2000; Hahn & Lunden, 2000; Essien, Radziemski, & Sneddon, 1988). A subset of this research has focused on the application of LIBS for detection and elemental analysis of aerosols, primarily for environmental monitoring (Carranza, Fisher, Yoder, & Hahn, 2001) and industrial emissions (Hahn, Flower, & Hencken, 1997). Other studies have focused on the application of LIBS for analysis of toxic species in aerosols collected on filters (Panne, Neuhauser, Theisen, Fink, & Niessner, 2001), or detection of trace elements in metals and metal alloys (Kim et al., 1997). In general however, most studies have concentrated on qualitative elemental analysis. Among the few attempts towards any quantitative LIBS analysis, was determination of trace elements in aluminum–lithium alloys by Gomba, D'Angelo, Bertuccelli, and Bertuccelli (2001).

Our focus in this paper is to develop the methodology to use LIBS to quantify the composition of multi-component aerosols without the need for materials standards. Our more specific need has been to have a tool to assess the extent of passivation on aluminum nanoparticles. The motivation for this work comes from the interest in the use of nano-aluminum for advanced propellants and energetic materials formulations. The specifics of studying the oxide content are related to both its function and manufacture. Obviously, in the latter case any bulk scale manufacturing process of nano- metals would be highly dangerous if conducted without some type of surface passivation. The most obvious coating material would be the native oxide, and it would be highly useful to have a tool to monitor the process. We recently demonstrated the ability to track oxygen content using a custom-built quantitative single-particle mass spectrometer (QSPMS) and extract the kinetics of Al nanoparticle oxidation exposed to air at various temperatures (Park, Lee, Rai, Mukherjee, & Zachariah, 2005). However, this technique, while powerful, is quite complex and may not be suitable as a routine characterization tool. Furthermore, the method relies on extraction of a sample which may not be feasible if spatially resolved measurements are desired, as for example in the characterization of the burning of aluminum.

Here, we will use LIBS for in situ quantitative spectrochemical analysis to predict the oxygen content in aluminum nanoparticles oxidized in air at various temperatures. The method employs obtaining time-resolved atomic emission spectra and plasma temperature. In order to obtain a quantitative measure of relative species populations in the aerosol, we also develop a calibration scheme in which the measured population densities of the background gas (argon) is used as an internal calibration standard. This latter step then enables a quantitative determination on the population densities without the need for reference materials.

## 2. Experimental approach

### 2.1. LIBS system

The LIBS experimental system is illustrated in Fig. 1(a). A laser-induced plasma is created with a Q-switched Nd:YAG laser ($\lambda = 1064$ nm) operated at an energy of 350 mJ/pulse at 10 Hz, and a pulse width of 4 ns. The beam is focused with a 100 mm focal length fused silica plano-convex lens (diameter = 50 mm) to provide an estimated fluence of $\sim$10–15 GW/cm$^2$ at the focal point. For such laser energy densities one can expect a breakdown at 1 atm to produce a micro-plasma of approximately 1–2 mm$^3$ with peak temperatures of 20,000–25,000 K. An aerosol flow exits a nozzle placed approximately 1 mm below the plasma breakdown.

The plasma fluorescence is collected in the back-scattered direction with the same focusing lens, and then re-focused with a 250 mm focal length lens to the entrance slit of a 0.5 m 1200 grooves/mm grating Czerny-Turner spectrometer (Acton SpectraPro 500i), with a resolution of 0.05 nm at 435.8 nm

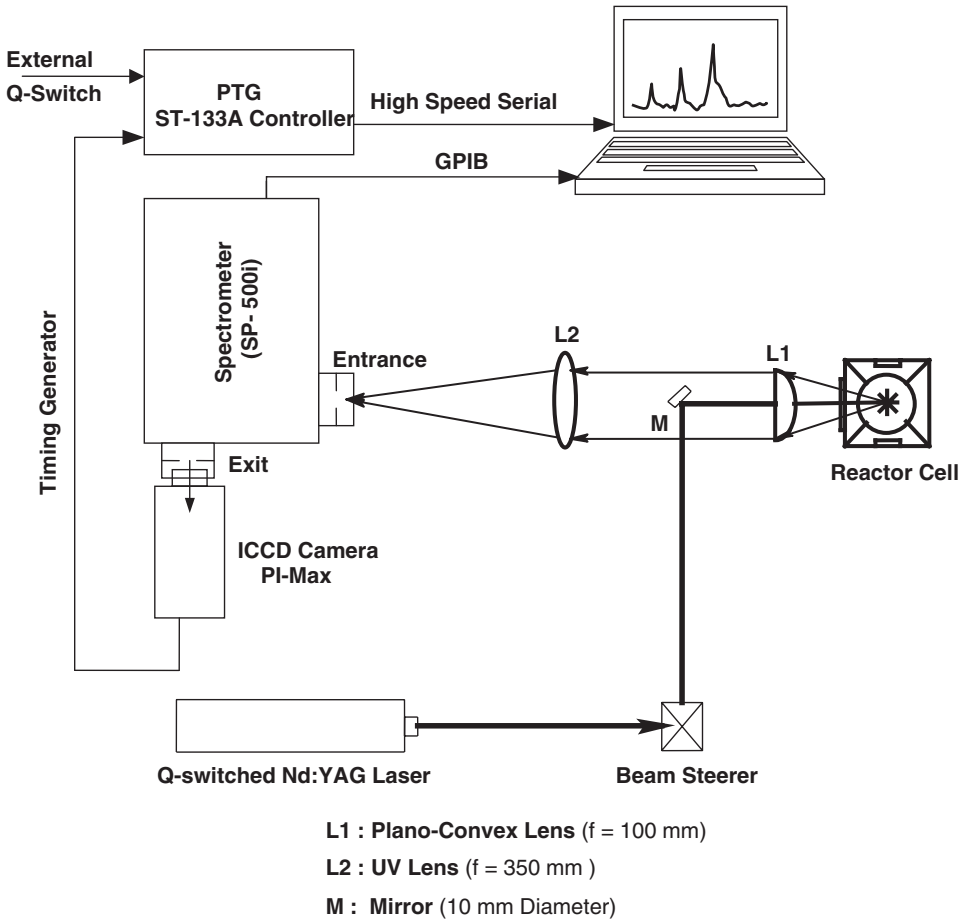


Fig. 1(a). Schematic for LIBS experimental system.

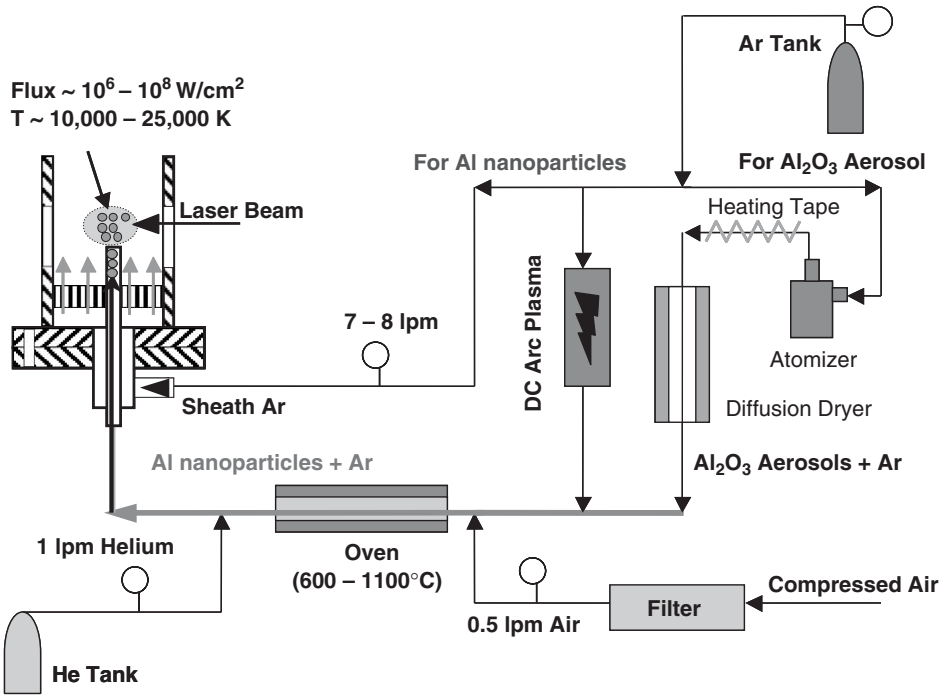


Fig. 1(b). Schematic for aerosol supply system.

wavelength, and a nominal dispersion of 1.7 nm/mm. The slit width for all experimental runs was kept at 0.23 mm for optimal signal intensity and spectral line widths. The dispersed spectra are recorded at the exit focal plane of the spectrometer with a time-gated intensified charge-coupled device (ICCD) detector array (Princeton Instruments Pi-MAX; Thomson 512 × 512 CCD) with an effective linear dispersion of approximately 0.023 nm/pixel. The gate trigger was supplied from the laser Q-switch. The absolute signal intensities were corrected for the effective transmission efficiency calculated from the photocathode quantum and diffraction grating efficiencies.

### 2.2. Aerosol generation

The aerosol generation and supply has been schematically represented in Fig. 1(b). We use two parallel aerosol generation systems. The first set-up delivers $Al_2O_3$ aerosols (an aerosol with known stoichiometry) to validate the calibration technique and data analysis methodology. The $Al_2O_3$ particles with a median particle diameter of 70–80 nm (Avocado Inc.) were suspended in de-ionized water with a magnetic stirrer, and aerosolized in an inert gas medium of argon with an atomizer. The aerosols are then freed of moisture by passing through a heated tube, and two successive silica gel diffusion dryers. In the second set-up, we use a home-built DC arc plasma reactor to generate Al nanoparticles. The DC arc method is shown in Fig. 2 and is essentially an evaporation–condensation method. A DC plasma arc is ignited between aluminum pellets housed in a carbon boat (Sigma-Aldrich Inc. 99.99%) that serves as the anode, and a tungsten wire cathode, to provide the energy for the evaporation of aluminum. An infinite amperes DC arc welder served as the power source for the system. The arc was operated with the voltage ranging

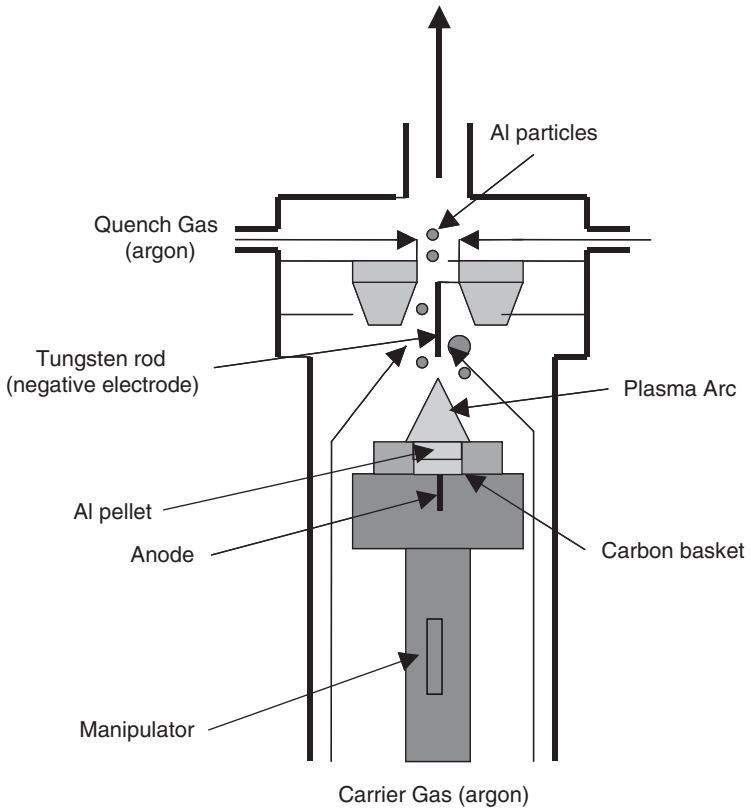


Fig. 2. Schematic diagram for DC arc plasma source used for Al nanoparticle generation.

from 11 to 15 V, and current ranging from 35 to 45 A, so as to maintain a steady production of aluminum nanoparticles. Argon was used as a carrier gas (6–7 LPM) for the aluminum vapor, and was also used as a quench gas (∼20 LPM) to facilitate the condensation of aluminum vapor to form nanoparticles. The typical size distribution of Al nanoparticles obtained from the DC arc source can be seen from Fig. 3, which plots particle number concentration as a function of the particle mobility diameter. Fig. 3 shows that the mean mobility diameter of the generated aerosols range between 50 and 75 nm with a peak concentration of $2E + 6$ #/cm$^3$. A part of the aerosol flow (about 4–5 LPM) is then mixed with 0.5 LPM of air before being fed to a heated flow tube for oxidation. For a given residence time inside the flow tube (∼1 s), the extent of oxidation for the nanoparticles is controlled by varying temperatures between 600 and 1100 °C. The optimal air flow rate ensured that sufficient oxygen was supplied to oxidize the small volume loading of Al nanoparticles, while keeping the amount of background oxygen in the flow stream to a minimum. The uniformity in the experimental procedure was maintained by keeping an identical mixture of Ar, He and the same quantity of air flow in the buffer gas for all experiments, including those of the $Al_2O_3$ aerosols, and blank background spectra of buffer gas without any aerosols. In both set-ups, the aerosol stream was further mixed with 1 LPM of helium, for reasons to be discussed later, before being introducedinto the laser probe volume in the reactor cell. The aerosols are finally injected into a reactor cell through a 1 mm diameter stainless steel tube as shown in Fig. 1(b). To prevent any contamination from the surroundings, the aerosol injector tube is embedded in a honeycomb mesh through which a sheath

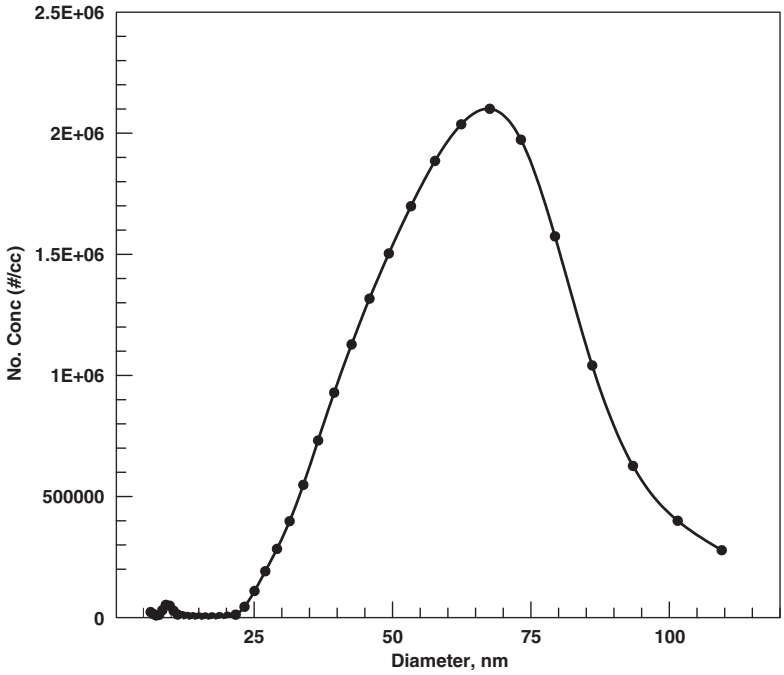


Fig. 3. Plot of particle number concentration (#/cm$^3$) versus particle diameter (nm) for Al nanoparticles generated from the DC arc plasma source.

flow of argon blankets the aerosol injector at the center of the cell (Fig. 1(b)). The background signals collected without any aerosols enable easy identification of required analyte signal from background noise, as well as efficient background subtraction from respective spectral signatures.

## 3. Methodology for spectral data analysis

In the present experiment time-resolved aluminum (Al I at 396.15 nm (Carranza et al., 2001)) and oxygen (O I at 777.2 nm (NIST Atomic Energy Levels Data Center, 1999)) atomic emission lines were recorded following the laser-induced plasma initiation. These spectral lines were chosen based on their relative strengths, accuracies and transition probabilities as listed by the NIST-Atomic Database (1999). Spectral details for the Al I and O I transition lines have been listed in Table 1. We validated the present

Table 1
Spectral database for Al I (396.15 nm) and O I (777.2 nm) transition lines chosen for the calculation of respective population densities, $N_i^{\mathrm{Al\ I}}$ and $N_i^{\mathrm{O\ I}}$ at 46.7 and 10.2 μs delay times

| Species | $\lambda$ (nm) | $A_{ki}$ ($s^{-1}$) | $E_k$ (eV) | $E_i$ (eV) | $\Delta E_{ki}$ (J) | $g_k$ | $g_i$ |
|---|---|---|---|---|---|---|---|
| Al I | 396.15 | 9.8e+7 | 3.1427 | 0.0138 | 5.01e−19 | 2 | 4 |
| O I | 777.1944 | 3.69e+7 | 10.7409 | 9.1460 | 2.56e−19 | 7 | 5 |

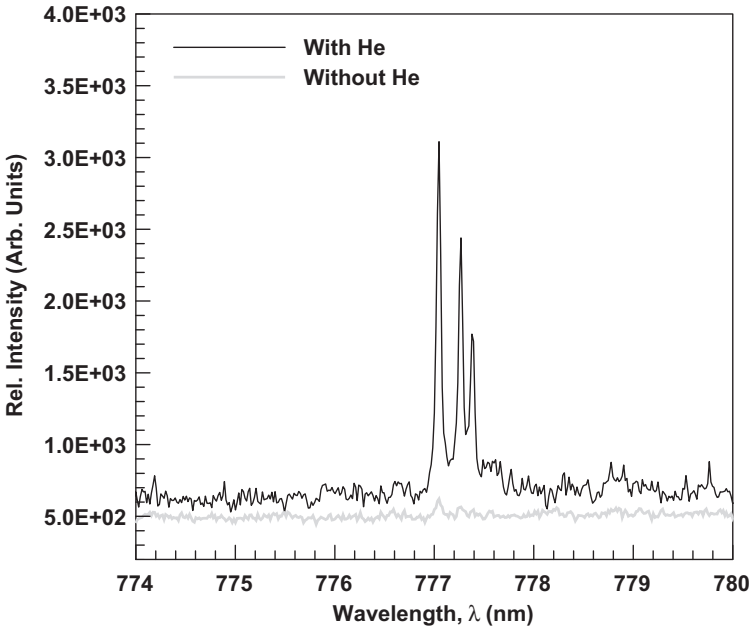


Fig. 4. Enhanced O I (777.2 nm) emission lines due to addition of 1 LPM of helium to the background gas of argon. The spectrum for "Without He" case has been shifted down on the scale for ease of comparison.

quantitative analysis from LIBS atomic emissions data by establishing known stoichiometries ($S =$ [O]/[Al]) for fully oxidized $Al_2O_3$ particles and pure Al (theoretically, $S = 1.5$ and 0, respectively) as our standard reference points. Then using an identical methodology, a series of spectral data were collected and analyzed to determine the oxygen content in DC arc plasma-generated Al nanoparticles systematically oxidized with air at temperatures of 600–1100 °C.

The use of argon as the buffer gas (Tognoni, Palleschi, Corsi, & Cristoforetti, 2002) offers the advantage that it produces a long radiative lifetime at atmospheric pressure, and produces the relatively high free electron densities and plasma temperatures required for local thermal equilibrium (LTE). The use of helium as background gas was found to enhance the otherwise weak signals of O I neutrals from the aerosols as demonstrated in Fig. 4 by the respective plots of O I signals collected for $Al_2O_3$ aerosols in buffer gas media with and without helium. Earlier studies (Lee et al., 1992; Griem, 1974) have also shown that at atmospheric pressure, He lowers the background continuum noise, and thereby enhances the signal/noise ratio. Due to the higher ionization potential and thermal conductivity of helium, it creates a less dense plasma with a lower electron density. The result is an enhanced signal due to a smaller self-absorption, and a lower background continuum due to weaker Bremsstrahlung radiation.

Fig. 5 is a flowchart that indicates the methodology used to quantitatively determine the elemental composition from LIBS spectra. Determination of O I and Al I population densities begins with collection of time-resolved O I and Al I spectral emissions for several gate delays ranging from 1.5 to 30 μs and 15 to 100 μs, respectively. These spectra are shown in Fig. 6 (a) and (b) for the case of $Al_2O_3$ aerosols. For all spectral data collected in the present work, each individual spectrum as shown in Fig. 6(a) and (b) is an average over 200 laser shots.

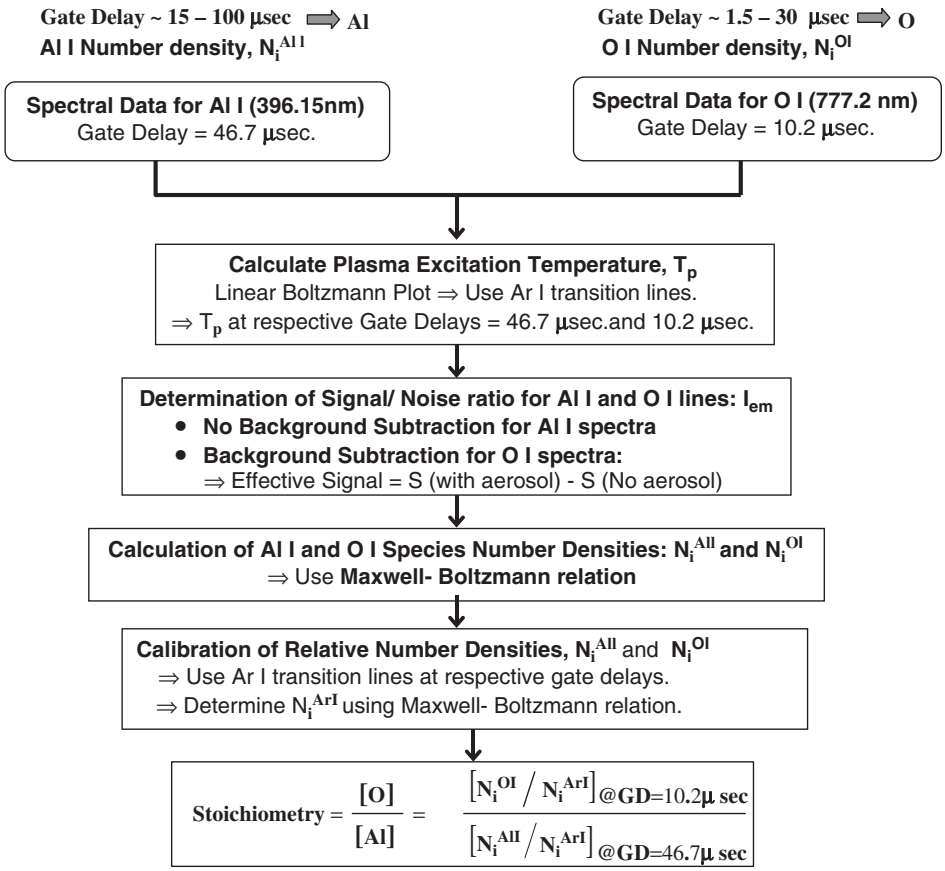


Fig. 5. Flow chart showing the methodology for quantitative spectral data analysis.

### *3.1. Spectral data for Al I and O I*

Fig. 6(a) and (b) indicate that for O I and Al I spectral data analysis, the ideal delay times should be chosen so that the background continuum is minimal and signal intensities are still relatively strong, resulting in high signal-to-noise ($S/N$) ratio. As suggested by Milan, Vadillo, and Laserna (1997), we take advantage of the fact that the laser preferentially couples with the aerosols, thereby making the signals from the aerosols more prominent above the background. The $S/N$ ratio was estimated by considering the ratio of peak intensity at the specified wavelength to the root mean square value of the noise, where the noise was calculated by considering 40 pixels along the baseline adjacent to the analyte peak. This enabled us to identify oxygen spectral signatures from the aerosols with minimal background interferences for gate delay times longer than 5 μs. At these late gate delays a significant increase in oxygen signals with the introduction of aerosol was noticed, indicating that this contribution came from oxidized Al nanoparticles. Based on the best $S/N$ ratio, the oxygen (O I at 777.2 nm) emission lines were acquired at a gate delay = 10.2 μs and gate width = 3.5 μs. For the case of aluminum, time-resolved Al I (396.15 nm) neutral emission lines recorded for $Al_2O_3$ aerosols, as shown in Fig. 6(b), indicated that the optimal set-up to maximize $S/N$ was at a gate delay of 46.7 μs and gate width of 15.5 μs.

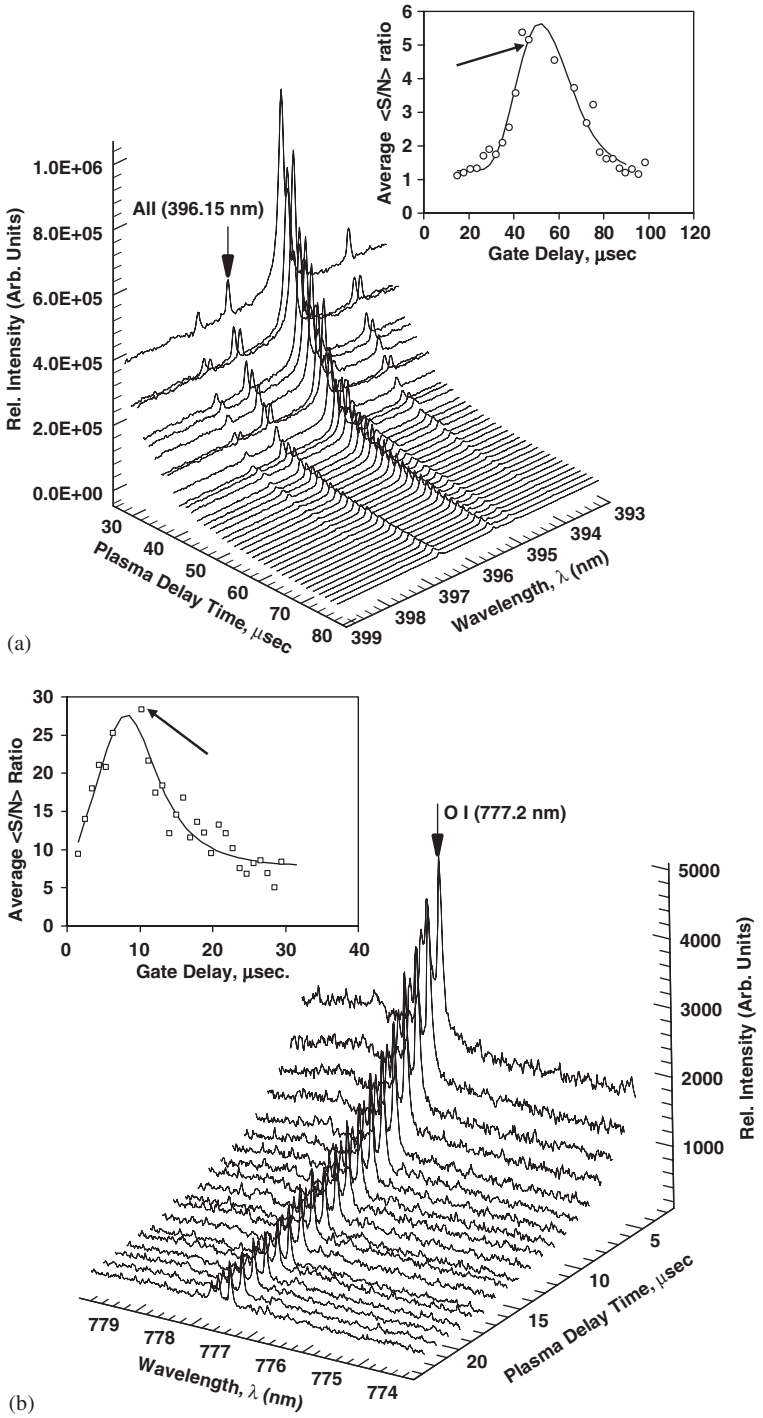


Fig. 6. Typical time-resolved atomic emission spectra of (a) Al I (396.15 nm) and (b) O I (777.2 nm)collected from laser-induced breakdown of $Al_2O_3$ aerosol. Gate delays range (a) 30–80 µs and (b) 5–25 µs. The inset figure shows the variation of average signal/noise ratio ($\langle S/N \rangle$) with gate delay times with the arrow indicating the optimal gate delay time chosen. The solid line indicates the best fit to the experimental data.

To calculate relative population densities of oxygen and aluminum from Boltzmann relations, the effective signals are taken as the normalized ratio of analyte peak intensity to baseline intensity (i.e., $S/N$ ratio) and, therefore, were independent of the absolute intensities. For all other analysis requiring absolute signal intensities, such as the plasma temperature determined from Boltzmann plots, and the relative population density calculation for the background Ar, absolute line intensities were corrected for corresponding wavelength-dependent transmission/detection efficiencies. As indicated in the flowchart in Fig. 5, with the known effective signal intensities $I_{\mathrm{em}}(=S/N)$, our next step required calculation of plasma temperature $T_{\mathrm{p}}$ at the respective delay times considered.

### 3.2. Plasma temperature measurement

The plasma temperatures were calculated based on the Boltzmann equation under the assumption of local thermal equilibrium (LTE). The conditions satisfying the assumption of LTE requires that the radiative-population rates are negligible compared to the collisional-population rates (Griem, 1964). This essentially implies that an excited state must have a higher probability of de-excitation by collision than by spontaneous radiation (Thorne, 1988). According to Radziemski et al. (1983), LTE generally is established among all the species in the plasma beyond 1 μs delay time from the plasma initiation. Given that our delay times are 10.2 μs and 46.7 μs for O I and Al I, respectively, we operate under an assumption of LTE. With LTE the plasma temperature is readily calculated from the Boltzmann equation relating the absolute emission intensities from two transitions $I_1$ and $I_2$ as

$$\frac{I_1}{I_2} = \frac{g_1 A_1 \lambda_2}{g_2 A_2 \lambda_1} \exp\left[-\frac{E_1 - E_2}{k_{\mathrm{B}} T_{\mathrm{exc}}}\right], \tag{1}$$

where $A_1$ and $A_2$ are the transition probabilities for any two transitions considered, $\lambda_1$ and $\lambda_2$ are the transition wavelengths, $g_1$ and $g_2$ are the statistical weights of the upper levels of the two transitions, $E_1$ and $E_2$ are the energies of the upper states, and $T_{\mathrm{exc}}$ is the plasma temperature at a given delay time. Since this relationship is linear, it can be extended to multiple lines by relating their intensities by plotting $\ln(I\lambda/gA)$ as a function of the upper state energy, $E_k$ (Yalcin et al., 1999). The linear fit to this plot generates a slope of $(-1/k_{\mathrm{B}}T_{\mathrm{exc}})$, from which the plasma temperature can be estimated.

### 3.3. Determination of species number density in plasma

For known plasma excitation temperatures $T_{\mathrm{exc}}$ and emission intensities $I_{\mathrm{em}}$ ($S/N$ ratio), we can proceed to calculate species population densities. Under the assumption of LTE, as discussed earlier, the relative population densities of O I and Al I species from the samples injected into the plasma were calculated based on the Boltzmann equation (sometimes referred to as Maxwell–Boltzmann equation) (Lee, Song, & Sneddon, 2000)

$$I_{\mathrm{em}} = A_{ki} h \nu_{ki} N_i \frac{g_k}{g_i} \exp\left(-\frac{\Delta E_{ki}}{k_{\mathrm{B}} T_{\mathrm{p}}}\right), \tag{2}$$

where $A_{ki}$ is Einstein's transition probability for the given transitions, $\nu_{ki}$ is the frequency of the transition, $g_k$ and $g_i$ are the respective statistical weights for upper state $k$ and lower state $i$, $\Delta E_{ki}$ is the energy difference in joules between the $k$ and $i$ states, and $h$ and $k_{\mathrm{B}}$ are Planck's and Boltzmann's constant, respectively. The respective plasma excitation temperature at given gate delays are defined as $T_{\mathrm{exc}}$ while

Table 2
List of Ar I transition lines and their spectral databases (NIST Atomic Spectra Database, 1999) used for plasma temperature calculation and calibration of oxygen (O I) and aluminum (Al I) population densities

| Species | $\lambda$ (nm) | Rel. int. | Accuracy | $E_k$ (eV) | $E_i$ (eV) | $A_{ki}$ (1/s) | $g_k$ | $g_i$ |
|---|---|---|---|---|---|---|---|---|
| Ar I | 415.859 | 400 | C | 14.5289 | 11.5484 | 1.40e+06 | 5 | 5 |
| Ar I | 420.068 | 400 | C | 14.4991 | 11.5484 | 9.67e+05 | 7 | 5 |
| Ar I | 425.936 | 200 | C | 14.7381 | 11.8281 | 3.98e+06 | 1 | 3 |
| Ar I | 427.217 | 150 | C | 14.5249 | 11.6236 | 7.97e+05 | 3 | 3 |
| Ar I | 433.356 | 100 | C | 14.6883 | 11.8281 | 5.68e+05 | 5 | 3 |
| Ar I | 451.073 | 100 | C | 14.576 | 11.8281 | 1.18e+06 | 1 | 3 |
| Ar I | 603.213 | 70 | C | 15.1305 | 13.0757 | 2.46e+06 | 9 | 7 |
| Ar I | 675.283 | 150 | C | 14.7425 | 12.907 | 1.93e+06 | 5 | 3 |
| Ar I | 696.543 | 10,000 | C | 13.3279 | 11.5484 | 6.39e+06 | 3 | 5 |
| Ar I | 706.722 | 10,000 | C | 13.3022 | 11.5484 | 3.80e+06 | 5 | 5 |

$N_i$ is the number density of each species at the lower states at a given time. In the present study, the number densities shall be referred to as $N_i^{\mathrm{O\ I}}$ and $N_i^{\mathrm{Al\ I}}$ for oxygen and aluminum, respectively.

### 3.4. Calibration of relative species number density with an internal standard

The population densities for the oxygen ($N_i^{\mathrm{O\ I}}$) and aluminum ($N_i^{\mathrm{Al\ I}}$) species, as discussed earlier, were determined from the Boltzmann equation (Eq. (2)) by using the relative spectral emission intensities recorded at specific time delays for a given spectrometer and camera set-up. Factors such as spectrometer and camera slit width, and the specific optical alignment for the experiment will affect both the absolute and relative emission signals observed. Furthermore, the absolute and relative intensities of atomic emission lines are related to the plasma temperature, which for our case are different for Al I and O I as they are taken at different gate delays. Thus, in order to obtain a quantitative estimation of oxygen content in the oxidized Al nanoparticles (namely, the population densities for both Al I and O I species), we calibrate the system with respect to a standard population density of a bulk species in the plasma. In the present experiment we used an internal calibration standard such that Al I and O I species emissions were normalized by the respective population densities of Ar ($N_i^{\mathrm{Ar\ I}}$), obtained at the respective delay times of 10.2 and 46.7 μs for the same experimental set-up.

For each of the aerosol samples used for the oxidation study, a series of 10 Ar I transition lines were collected at the respective time delays chosen for the Al I and O I emissions. One advantage of keeping argon as the inert gas environment is that there are ample strong Ar I neutral emissions over a wide range of wavelengths that span over long time intervals of the plasma evolution. The Ar I atomic emission lines used here for the calibration were chosen based on their relative strengths and accuracies as obtained from NIST-Atomic Spectral Database (1999). All Ar I lines used for calibration purposes have been listed in Table 2. Thus for the [O]/[Al] ratio, the normalization procedure can be expressed as

$$\text{Stoichiometry} = \frac{[\mathrm{O}]}{[\mathrm{Al}]} = \frac{[N_i^{\mathrm{O\ I}}/N_i^{\mathrm{Ar\ I}}]_{@\ \mathrm{GD}=10.2\,\mu\mathrm{s}}}{[N_i^{\mathrm{Al\ I}}/N_i^{\mathrm{Ar\ I}}]_{@\ \mathrm{GD}=46.7\,\mu\mathrm{s}}}. \tag{3}$$

Such a calibration technique enables one to determine relative number densities of atomic species of interest from independent spectral data collected at different time delays and plasma conditions, provided they are normalized by equivalent number densities of a bulk plasma species at the identical experimental conditions.

The discussion above outlines one approach for quantification of atomic densities. We briefly outline another approach, which we also found to provide quantitative results but which is more complex and therefore not as attractive. Without the addition of helium a pure argon background showed no O I neutral lines as a result of rapid recombination processes (Gleason & Hahn, 2001). This led us to monitor the ionic lines of O IV (328.65 nm) at much shorter delay times of 200–900 ns when ionic emission lines are prominent. Calibration of the relative population density of O IV species required determination of ground state Ar I population densities from Ar II ionic emission lines since at these earlier delay times one could only capture the ionic transitions. This in turn required calculation of electron density, which we determined by measuring the Stark broadened emission lines of Ar II (387.5 nm) for which Stark effects are strong and broadening parameters are known (Griem, 1974). This enabled us to calculate relative population densities of Ar I neutrals from Ar II by using the measured electron density, and the combined Saha and Boltzmann equation. The reduction in ionization energy due to the Debye shielding effect as a result of electron clouding in the early stages of the dense plasma was also taken into consideration (Griem, 1964; Thorne, 1988). While feasible, this method involved a lot more complexity and uncertainty in the calculation of ionization energy reduction, and absolute electron densities from Stark broadened lines. Furthermore the spectral lines for O IV collected at these earlier delay times had weak $S/N$ ratios due to large background continuum, so that the signal strengths were sufficient in the case of $Al_2O_3$ aerosols, but become progressively worse for the partially oxidized Al nanoparticles.

## 4. Results and discussion

### *4.1. Spectral analysis*

Due to ubiquitous presence of oxygen, we initially acquired a set of temporally resolved spectral emission for the blank background. In this case, we collected the spectral signals for only the carrier gas mixture of Ar, He and trace air in the absence of any aerosols for identical gate delay and spectrometer settings as subsequent measurements with aerosols. Recall from our prior discussion that the relatively weak signals of O I neutral emissions were enhanced, as shown in Fig. 4, with the addition of 1 LPM flow of He into the buffer gas stream of Ar. We also verified that when averaged over many hundreds of shots, the plasma temperature calculated with and without the aerosols for the same delay time in the laser probe volume exhibited little difference. This enabled us to subtract the blank background of the carrier gas mixture without any aerosols from the O I (777.2 nm) signals obtained with aerosols in the system for the same gate delay. This yields the net contribution in the O I peak intensity from the aerosols. From this net spectral database, we could obtain the signal for oxygen. The net background subtracted signal intensity along with the spectral signatures of O I emission lines with and without the aerosols has been shown in Fig. 7 for $Al_2O_3$ particles used as the fully oxidized reference point. Fig. 8 illustrates a typical Al I emission line, at a delay time of 46.7 μs, used for calculating the Al content in the particle. The complete absence of Al I at 396.15 nm in the background gas mixtures of Ar, He and air ensured that the source of the signal was only from the aerosol samples. This enabled us to directly measure the $S/N$ ratio from the analyte without the need for subtraction of the blank spectrum.

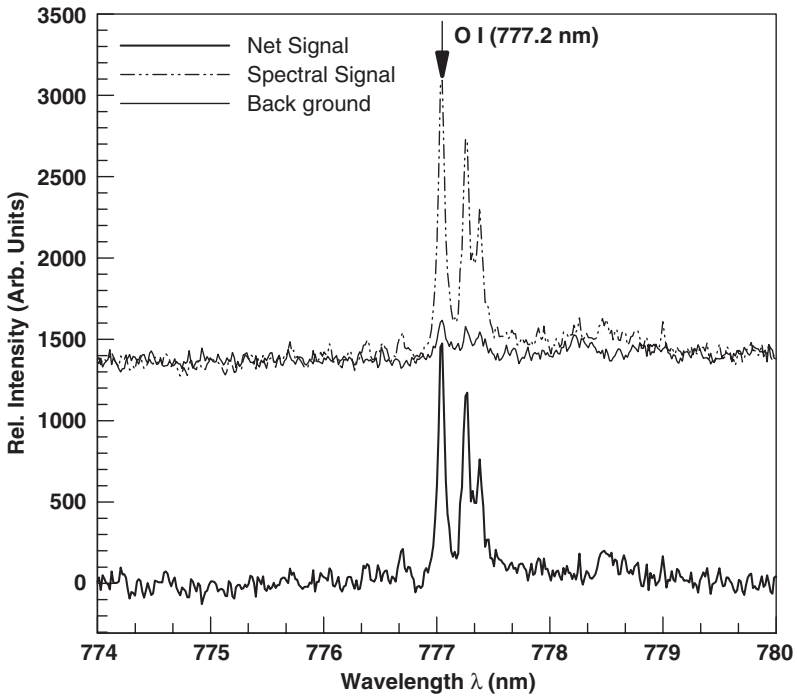


Fig. 7. Representative atomic transition line of O I (777.2 nm) collected for $Al_2O_3$ aerosols at delay time = 10.2 μs and gate width = 3.5 μs. The "Net Signal" spectrum indicates the background subtracted spectral signal intensity.

Similar sets of data were collected for aluminum nanoparticles oxidized by air at six different furnace temperatures ($T$ = 600, 700, 800, 900, 1000 and 1100 °C). Figs. 9 and 10 show the respective spectral signatures for Al I, and background subtracted signals for O I, collected from three different runs of oxidized Al nanoparticles heated in air at three representative temperatures of 700, 900 and 1100 °C. The corresponding plasma excitation temperatures ($T_{exc}$) have also been indicated for each of the cases of the Al I and O I spectra in the respective figures.

For all the oxidation cases studied here, plasma temperatures, $T_{exc}$, were calculated from Boltzmann linear plots based on Eq. (1) as described earlier. We used the absolute emission intensities for 5–7 Ar I neutral lines at two different time delays of the time-resolved spectra collected: (1) at 10.2 μs for the data analysis of O I atomic emission lines and (2) at 46.7 μs for the data analysis of Al I atomic emission lines. All Ar I transition lines chosen for the present work, along with their detailed spectral data, have been listed in Table 2. The choice of Ar I lines was based on (1) a relatively high strength and accuracy as listed by the NIST ASD (1999), (2) a wide energy spread to improve accuracy in the temperature measurement (Yalcin et al., 1999) and (3) significant signal intensities at the respective delay times considered. As the reference case, Fig. 11 shows the Boltzmann plot of $\ln(I\lambda/gA)$ versus normalized upper state energies ($E_k/k_B$) for seven strong emission lines of Ar I used to determine a plasma temperature of $T_{exc}$ = 10, 288 K, at a time delay of 10.2 μs, whereas Fig. 12 shows a similar plot for five Ar I emission lines whose slope gives a plasma temperature of $T_{exc}$ = 6603 K at a time delay of 46.7 μs. Similarly, plasma temperatures were measured for each of the conditions studied for the estimation of the oxygen content as a function of reactor temperature, and are listed in Table 3.

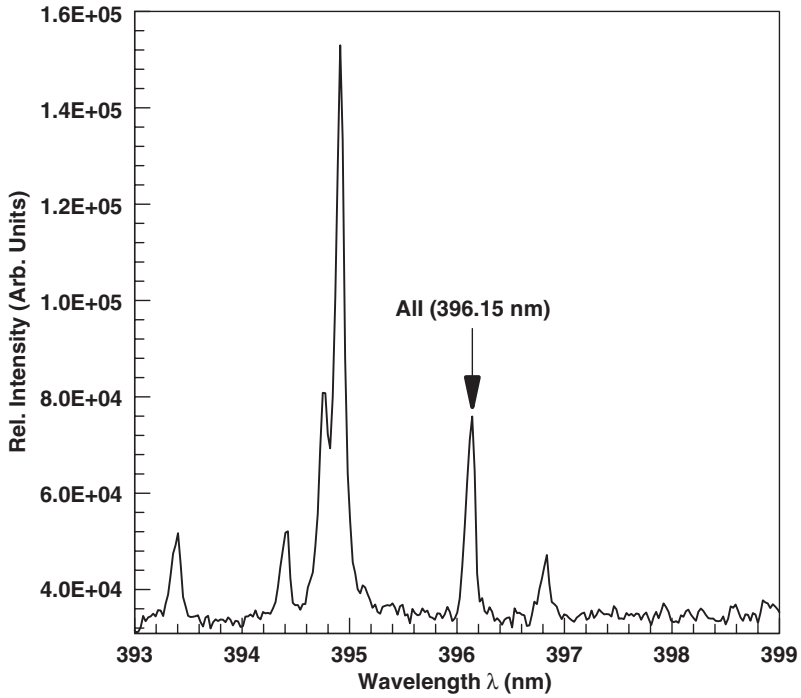


Fig. 8. Representative atomic transition line of Al I (396.15 nm) collected for $Al_2O_3$ aerosols at delay time = 46.7 μs and gate width = 15.5 μs.

Using Eq. (2) along with the known emission intensities, $I_{em}$, and plasma temperatures, $T_{exc}$ at delay times of 10.2 and 46.7 μs, the relative population densities of oxygen ($N_i^{O\ I}$) and aluminum ($N_i^{Al\ I}$) were estimated from the atomic emission lines of O I (777.2 nm) and Al I (396.15 nm). For all the cases, since the net oxygen emission intensities were obtained by subtracting the oxygen contribution from the background as discussed earlier and shown in Fig. 7, we used the $S/N$ ratio as the effective emission intensity ($I_{em}$) to calculate the relative species densities for both aluminum and oxygen. This ensured the uniformity of data used for quantitative analysis, since we are only interested in determining the ratio of oxygen to aluminum population density, i.e., [O]/[Al] ratio. Also, the use of normalized intensities ($S/N$ ratio) ensures that their magnitudes were independent of the absolute transmissions and the gate widths. This becomes crucial for the O I intensity values, since we only have information on the relative magnitude of its signal from background subtraction and not the absolute values. The respective transition probabilities $A_{ki}$, upper ($E_k$) and lower ($E_i$) state energies and the corresponding statistical weight factors ($g_k$ and $g_i$) for the Al I and O I transitions used were available from NIST (1999) and have been listed in Table 2.

Finally, as discussed earlier, artifacts due to the experimental set-up or temporal evolution of plasma volume were cancelled by calibrating the species number densities with the respective bulk Ar population densities calculated at identical plasma conditions from different Ar I emission lines as listed in Table 2.

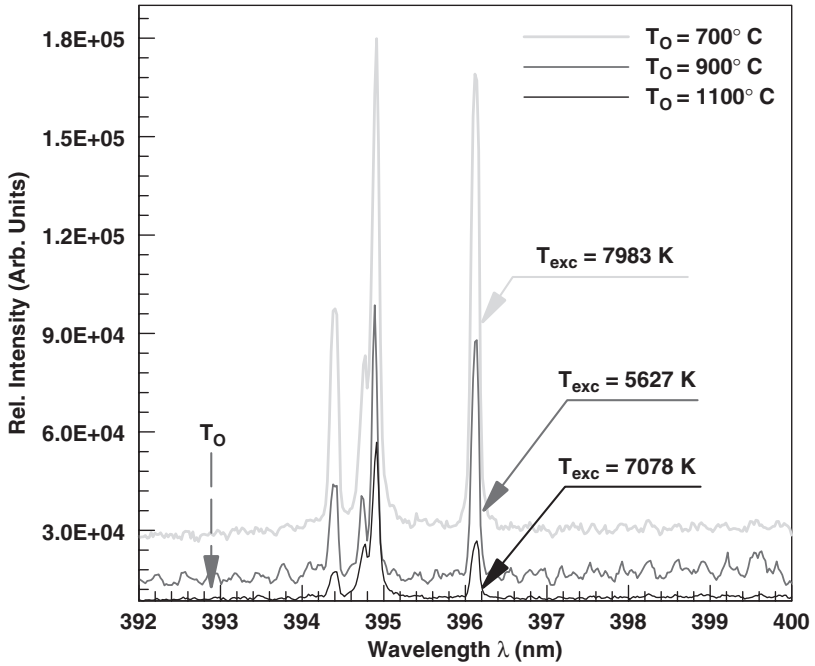


Fig. 9. Relative emission intensities of Al I (396.15 nm) signals collected at a delay time of 46.7 μs for Al nanoparticles oxidized at three different oven temperatures ($T_O = 700$, 900, 1100 °C). The respective plasma temperatures for each of the samples have been indicated as $T_{exc}$ (K). All spectra shown have been shifted along the $y$-scale for ease of visualization.

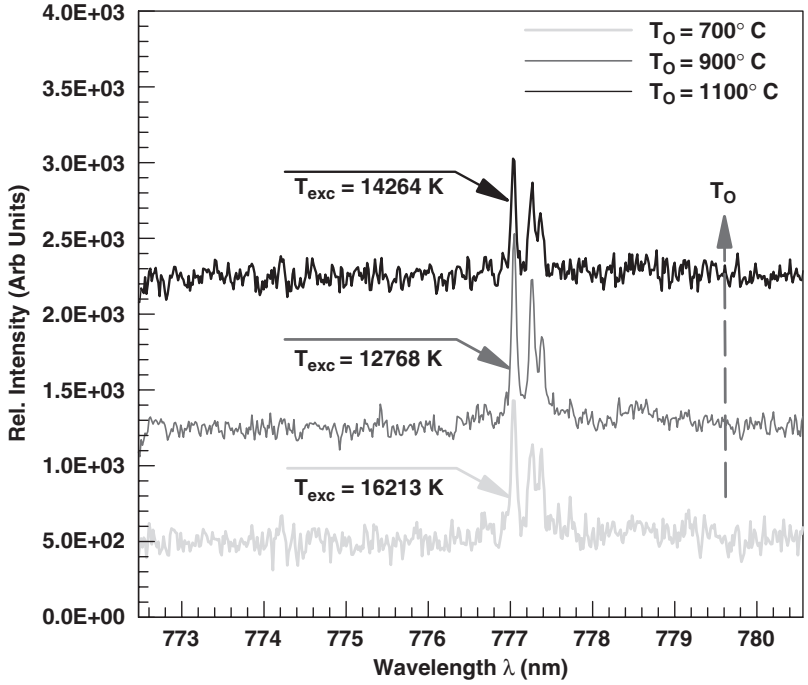


Fig. 10. Relative intensities of background subtracted net emission signals of O I (777.2 nm) at a delay time of 10.2 μs for Al nanoparticles samples oxidized at three different oven temperatures ($T_O = 700$, 900, 1100 °C). The respective plasma emperatures calculated at 10.2 μs delay time have been indicated as $T_{exc}$ (K). All spectra shown have been shifted along the $y$-scale for ease of visualization.

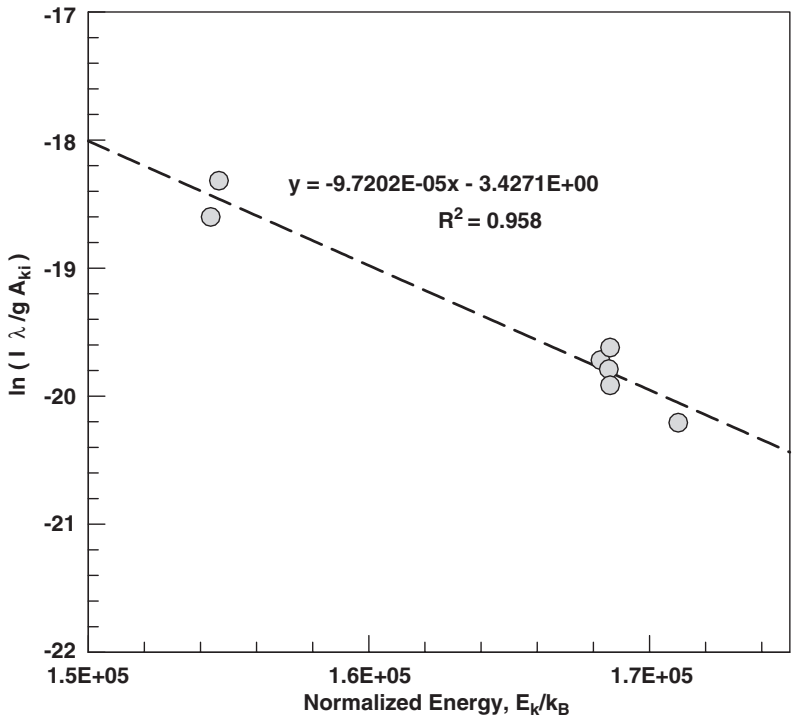


Fig. 11. Typical linear Boltzmann plot for seven Ar I transition lines used to calculate plasma temperature, $T_{exc}$, for estimating oxygen number densities in $Al_2O_3$ aerosol samples ($T_{exc} = 1/\text{slope} = 10,288$ K at delay time $= 10.2\,\mu$s). Plot also shows linear fit to the data with a regression coefficient of $R^2 \sim 0.958$.

### 4.2. Oxidation analysis

The [O]/[Al] ratios calculated from the present quantitative analysis along with their respective uncertainties for all the analyte samples studied have been listed in Table 3. It also shows the corresponding plasma excitation temperatures ($T_{exc}$) at time delays of 10.2 and 46.7 μs for each of the samples. As a typical example, the stoichiometry, [O]/[Al] ratio for the known case of $Al_2O_3$ aerosol samples was calculated from the LIBS data by using the calibration scheme described above and shown in Eq. (3) and was found to be $1.55 \pm 0.16$ (refer to "Al oxidized at 1100 °C" case in Table 3), in good agreement with the expected value of 1.5. All possible combinations of Ar I emission lines, as listed under Table 2, were considered to calculate population densities of Ar atoms used to normalize relative population densities of Al I and O I at the respective time delays in order to account for experimental uncertainties. The above result, for the known stoichiometry of $Al_2O_3$ aerosol samples, indicated that we could quantitatively determine the oxygen to aluminum ratio without the need of a material standard for calibration purposes.

There data can also be presented in terms of the extent of oxidation, α, from the following reaction:

$$2\text{Al} + \tfrac{3}{2}\alpha\text{O}_2 \rightarrow (1-\alpha)\text{Al} + \alpha\text{Al}_2\text{O}_3. \tag{4}$$

Here, the extent of oxidation, α, indicates the chemical reaction such that $\alpha = 1$ stands for complete oxidation of Al into $Al_2O_3$ whereas $\alpha = 0$ implies pure Al. All other values of α between 0 and 1 indicate partially oxidized Al nanoparticles, probably as an Al core covered by an oxide shell.

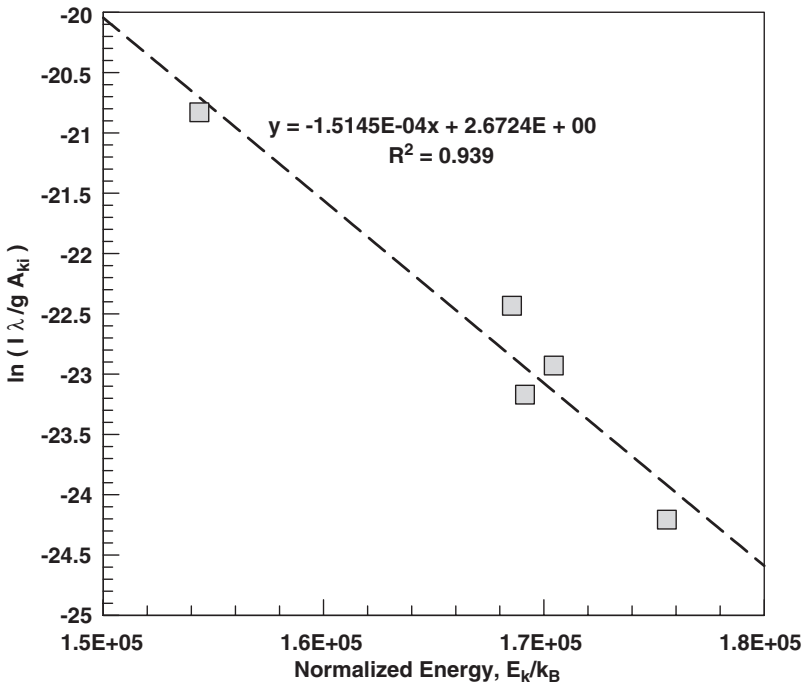


Fig. 12. Typical linear Boltzmann plot for five Ar I transition lines used to calculate plasma temperature, $T_{exc}$, for estimating aluminum number densities in $Al_2O_3$ aerosol samples ($T_{exc} = 1/\text{slope} = 6603$ K at delay time = 46.7 μs). Plot also shows linear fit to the data with a regression coefficient of $R^2 \sim 0.939$.

Table 3
Extent of conversion, α and [O]/[Al] ratios along with their experimental uncertainties and plasma temperatures at delay times of 10.2 and 46.7 μs

| Samples studied | $S = [O]/[Al]$ ratio | Extent of conversion, α | Plasma excitation temp. $T_{exc}$ (K)[a] | |
|---|---|---|---|---|
| | | | at 10.2 μs | at 46.7 μs |
| Pure Al | 0.05 ± 0.013 | 0.034 ± 0.009 | 21, 356 ± 2311 | 18, 422 ± 955 |
| Al oxidized at 600 °C | 0.34 ± 0.072 | 0.228 ± 0.048 | 10, 155 ± 591 | 6154 ± 663 |
| Al oxidized at 700 °C | 0.68 ± 0.103 | 0.456 ± 0.069 | 16, 213 ± 1033 | 7983 ± 794 |
| Al oxidized at 800 °C | 0.76 ± 0.121 | 0.509 ± 0.081 | 14, 457 ± 2421 | 7412 ± 755 |
| Al oxidized at 900 °C | 0.94 ± 0.134 | 0.628 ± 0.089 | 12, 768 ± 1911 | 5627 ± 383 |
| Al oxidized at 1000 °C | 1.03 ± 0.134 | 0.688 ± 0.089 | 29, 452 ± 3677 | 4915 ± 178 |
| Al oxidized at 1100 °C | 1.55 ± 0.158 | 1.036 ± 0.106 | 14, 264 ± 1908 | 7078 ± 705 |
| Pure $Al_2O_3$ | 1.56 ± 0.190 | 1.038 ± 0.127 | 10, 288 ± 960 | 6603 ± 969 |

[a]For all the cases studied, $T_{exc}$ values at 10.2 and 46.7 μs were used for population density calculation and calibration of O I and Al I species, respectively.

Fig. 13 plots the extent of conversion or oxidation of Al nanoparticles, α, as a function of various furnace temperatures (600–1100 °C) used for the oxidation of particles. The error bars indicate experimental uncertainties in α as propagated from those estimated for the [O]/[Al] ratio. Fig. 13 indicates that Al nanoparticles oxidized at a furnace temperature of 600 °C had undergone a relatively small extent of

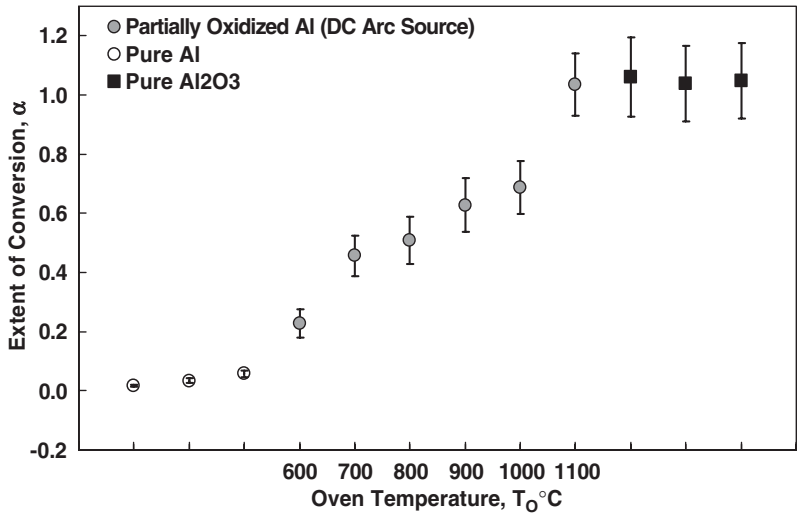


Fig. 13. Extent of oxidation in air, $\alpha$, of Al nanoparticles as a function of oxidation temperature. The oven temperature scale only extends between 600 and 1100 °C. Data points below 600 °C and above 1100 °C are for pure Al and $Al_2O_3$ aerosols used as reference points.

oxidation with $\alpha = 0.228 \pm 0.048$. On the other hand, at a furnace temperature of 1100 °C, the particles are essentially all converted to $Al_2O_3$ as indicated by $\alpha = 1.036 \pm 0.106$. The two benchmark case studies for the extent of oxidation of pure Al ($\alpha \sim 0.01$–$0.05$) and $Al_2O_3$ aerosols ($\alpha \sim 1.03$–$1.06$) measured for three different experimental runs were also plotted on the same figure outside the furnace temperature range of 600–1100 °C. These samples indicate that good agreement for particle stoichiometry can be achieved through the use of an internal calibration process as described in this paper. It also suggests that the LIBS approach can be used as an on-line characterization tool to assess the extent of oxidation during particle passivation, and should be extendable to other coating processes and materials.

## 5. Conclusion

In this study we demonstrate the quantitative implementation of LIBS for the characterization of nano-aerosols. In particular by using the carrier gas, Ar as an internal standard, we are able to determine the extent of oxidation of aluminum nanoparticles. The approach involves finding the optimal laser delay time to collect spectra for each of the elemental species of interest, and measuring the plasma temperature and argon density under the same conditions. This enabled us to nullify effects due to different experimental conditions, species excitation from different energy states or temporal evolution of the plasma volume itself. We used this procedure to calculate the extent of oxidation of aluminum nanoparticles as a function of furnace temperature.

## Acknowledgements

Support for this work comes from the ARMY-DURINT Center for NanoEnergetics Research (CNER) and the University of Maryland Center for Energy Concepts Development (CECD).

## References


Carranza, J. E., Fisher, B. T., Yoder, G. D., & Hahn, D. W. (2001). On-line analysis of ambient air aerosols using laser-induced breakdown spectroscopy. *Spectrochimica Acta Part B: Atomic Spectroscopy*, *56*, 851–864.

Damon, E. K., & Thomlinson, R. G. (1963). Observation of ionization of gases by a ruby laser. *Applied Optics*, *2*, 546–547.

Essien, M., Radziemski, L. J., & Sneddon, J. (1988). Detection of cadmium, lead and zinc in aerosols by laser-induced breakdown spectroscopy. *Journal of Analytical Atomic Spectrometry*, *3*, 985–988.

Gleason, R. L., & Hahn, D. W. (2001). The effects of oxygen on the detection of mercury using laser-induced breakdown spectroscopy. *Spectrochimica Acta Part B: Atomic Spectroscopy*, *56*, 419–430.

Gomba, J. M., D'Angelo, C., Bertuccelli, D., & Bertuccelli, G. (2001). Spectroscopic characterization of laser induced breakdown in aluminum–lithium alloy samples for quantitative determination of traces. *Spectrochimica Acta Part B: Atomic Spectroscopy*, *56*, 695–705.

Griem, H. R. (1964). *Plasma spectroscopy*. New York: McGraw-Hill.

Griem, H. R. (1974). *Spectral line broadening by plasmas*. New York: Academic Press.

Hahn, D. W., Flower, W. L., & Hencken, K. R. (1997). Discrete particle detection and metal emissions monitoring using laser-induced breakdown spectroscopy. *Applied Spectroscopy*, *51*(12), 1836–1844.

Hahn, D. W., & Lunden, M. M. (2000). Detection and analysis of aerosol particles by laser-induced breakdown spectroscopy. *Aerosol Science and Technology*, *33*, 30–48.

Hanafi, M., Omar, M. M., & Gamal, Y. E. E. D. (2000). Study of laser-induced breakdown spectroscopy of gases. *Radiation Physics and Chemistry*, *57*, 11–20.

Kim, D. E., Yoo, K. J., Park, H. K., Oh, K. J., & Kim, D. W. (1997). Quantitative analysis of aluminum impurities in zinc alloy by laser-induced breakdown spectroscopy. *Applied Spectroscopy*, *51*(1), 22–29.

Lee, Y.-I., Song, K., & Sneddon, J. (2000). *Laser induced breakdown spectrometry*. Huntington, NY: Nova Science Publishers.

Lee, Y.-I., Thiem, T. L., Kim, G.-H., Teng, Y.-Y., & Sneddon, J. (1992). Interaction of an excimer-laser beam with metals. Part III: The effect of a controlled atmosphere in laser-ablated plasma emission. *Applied Spectroscopy*, *46*(11), 1597–1604.

Martin, M., & Cheng, M.-D. (2000). Detection of chromium aerosol using time-resolved laser-induced plasma spectroscopy. *Applied Spectroscopy*, *54*(9), 1279–1285.

Meyerand, R. G., Jr., & Haught, A. F. (1963). Gas breakdown at optical frequencies. *Physical Review Letters*, *11*, 401–403.

Milan, M., Vadillo, J. M., & Laserna, J. J. (1997). Removal of air interference in laser-induced breakdown spectrometry monitored by spatially and temporally resolved charge-coupled device measurement. *Journal of Analytical Atomic Spectrometry*, *12*, 441–444.

Minck, R. W. (1964). Optical frequency electrical discharges in gases. *Journal of Applied Physics*, *35*, 252–254.

NIST Atomic Energy Levels Data Center. (1999). NIST Atomic Spectra Database, Physics Laboratory: National Institute of Standards and Technology. URL: http://physics.nist.gov/PhysRefData/ASD/index.html.

Panne, U., Neuhauser, R. E., Theisen, M., Fink, H., & Niessner, R. (2001). Analysis of heavy metal aerosols on filters by laser-induced plasma spectroscopy. *Spectrochimica Acta Part B: Atomic Spectroscopy*, *56*, 839–850.

Park, K., Lee, D. G., Rai, A., Mukherjee, D., Zachariah, M. R., 2005. Size-resolved kinetic measurements of aluminum nanoparticle oxidation with single particle mass spectrometry. *Journal of Physical Chemistry B*, *109*, 7290–7300.

Radziemski, L. J., & Cremers, D. A. (1989). Spectrochemical analysis using laser plasma excitation. In: L.J. Radziemski, & D.A. Cremers (Eds.), *Laser-induced plasmas and applications* (pp. 6107–6118). New York: Marcel Dekker.

Radziemski, L. J., Loree, T. R., Cremers, D. A., & Hoffman, N. M. (1983). Time-resolved laser-induced breakdown spectrometry of aerosols. *Analytical Chemistry*, *55*, 1246–1252.

Thorne, A. P. (1988). *Spectrophysics*. New York: Chapman & Hall.

Tognoni, E., Palleschi, V., Corsi, M., & Cristoforetti, G. (2002). Quantitative micro-analysis by laser-induced breakdown spectroscopy: A review of the experimental approaches. *Spectrochimica Acta Part B: Atomic Spectroscopy*, *57*, 1115–1130.

Weyl, G. M. (1989). Physics of laser-induced breakdown: An update. In: L.J. Radziemski, & D.A. Cremers (Eds.), *Laser-induced plasmas and applications* (pp. 5978–5985). New York: Marcel Dekker.

Yalcin, S., Crosley, D. R., Smith, G. P., & Faris, G. W. (1999). Influence of ambient conditions on the laser air spark. *Applied Physics B*, *68*, 121–130.